Results in Engineering 4 (2019) 100054

Contents lists available at ScienceDirect

Results in Engineering

journal homepage: www.editorialmanager.com/rineng/Default.aspx

A modelling tool for engine and exhaust aftertreatment performance analysis in altitude operation

J.R. Serrano, P. Piqueras *, E.J. Sanchis, B. Diesel

CMT-Motores Térmicos, Universitat Politècnica de València, Camino de Vera S/n, 46022 Valencia, Spain

ARTICLE INFO

Keywords:
Internal combustion engine
Altitude
Emissions
Particulate matter
Aftertreament
Modelling

ABSTRACT

New regulation standards on engine pollutant emissions are widening the engine operating conditions subjected to type approval tests as a way to prevent from the gap between regulated and real-driving emissions. In this regard, ambient temperature and driving altitude are new boundaries to be considered. Although the basis of the impact of these variables has been studied concerning the engine performance, new challenges appear to meet the emission limits and the aftertreatment conversion efficiency. In this work, a gas dynamic modelling tool is approached to explore the maximisation of the engine torque when operating at high altitude in a wide range of ambient temperatures. Particular focus is put on the modelling of the combustion, the turbocharger and the exhaust aftertreatment system. Starting from a sea-level calibration, the proposed methodology accounts for mechanical criteria as well as the impact on the engine raw emissions and exhaust flow properties to define new combustion settings for altitude operation. Next, these boundaries are applied to the exhaust aftertreatment system to analyse the impact on the catalyst conversion efficiency and the particulate filter performance concerning pressure drop and filtration efficiency.

Introduction

Seeking to encompass the widest range of engine operation to assess the exhaust emissions from internal combustion in the scope of the pollutant standards, European regulations [1] include as main novelty real driving emission (RDE) tests with the altitude and the ambient temperature as additional boundary conditions. These tests have as main objective to encourage the implantation of systems and strategies able to respond adequately in terms of tailpipe emissions in real-world vehicle use. Therefore, not only the traditional engine components and processes [2] are to be improved but also the exhaust aftertreatment systems (ATS), both in compression ignition [3] and spark-ignition [4] engines.

RDE tests have been enacted by September 2017 and are executed to supplement laboratory tests, i.e. the Worldwide harmonized Light vehicles Test Cycle (WLTC) as a chassis dynamometer type approval test of the WLTP, as representative of a daily vehicle use [5]. During the RDE, NOx emissions must not exceed 2.1 times the allowable emissions under Euro 6d-Temp [6]. The tests cover altitudes from 0 to 700 m and ambient temperature ranging from $0°C$ to $30°C$ within the moderate range with allowable extension till 1300 m and -7 to $35°C$ accounting for an additional emissions corrective factor [5]. The aim is to incorporate common situation encountered in many regions accounting for the altitude factor since many populated cities are 1000 m over sea-level [7] facing a wide ambient temperature window.

Several studies have considered these further variables on emissions and performance. Luján et al. [8] analysed the impact of very low ambient temperature on the pollutant emissions of a Diesel engine during transient operation. Both raw HC and CO emissions were shown to be strongly affected by the reduction of the ambient temperature from $20°C$ to $-7°C$. The diesel oxidation catalyst (DOC) conversion efficiency was also affected, specially in the case of the CO conversion efficiency due to CO inhibition appearing in huge instantaneous emission related to transient load phases at $-7°C$ [9]. Faria et al. [10] used real-life driving data covering the moderate range for ambient temperature to quantify the emissions during cold starts in urban context. The results evidenced a clear penalty in fuel consumption and emissions during cold start in comparison to hot operation underlining how this is taking place locally in populated areas. In addition, higher damage was found for gasoline than for diesel vehicles. The impact of extreme cold weather conditions on 14 gasoline and diesel engines was also investigated by Weber et al. [11]. The effect of cold temperature was evidenced to be very significant on all pollutant emissions any the engine type. With a similar approach,

* Corresponding author.
E-mail address: pedpicab@mot.upv.es (P. Piqueras).

https://doi.org/10.1016/j.rineng.2019.100054
Received 23 August 2019; Received in revised form 24 October 2019; Accepted 30 October 2019

cold start and hot restart in winter season have been also compared in the work of Ko et al. [12] for Euro 5 and Euro 6 vehicles. The trend in the results is similar to that shown in other studies but reaching special interest the clearly lower emissions of NO_x in Euro 6 vehicles, what certifies the high performance of current NO_x reduction techniques. Ko et al. [13] have recently analysed the performance of lean NOx trap (LNT) systems in RDE tests. The consecutive acceleration and deceleration phases in urban areas showed negative effects on the LNT regeneration in contrast to rural and motorway driving, where the LNT regeneration occurred periodically improving the NOx conversion efficiency. Otherwise, it was evidenced that slight increases in ambient temperature (27C–33C) caused 55% higher NOx emissions.

As the altitude increases the air density is lower. Thereby the aspirated air mass flow is reduced impacting on a number of processes that determine a relevant change in the engine response [14]. An increase of fuel consumption and emissions is reported in all the studies related to the impact of increasing the driving altitude [15]. In addition, the decrease of the air density leads the control strategies to push the combustion and boost processes towards several mechanical limits looking for maximum power availability. The start of the injection (SOI) is commonly advanced leading to maximum in-cylinder pressure gradient and absolute value [16]. The boost system increases the exhaust manifold pressure. As a consequence, the pumping losses increase as well as the pollutants emissions related to in-cylinder exhaust backflows [14]. Although the boost system allows keeping the sea-level engine performance at low altitude, as this one increases the compressor moves towards the surge region and the turbocharger speed reaches its maximum value in full-load operation. Therefore, an altitude is reached from which the exhaust gas recirculation (EGR) path has to be closed to provide the combustion chamber with as much fresh air as possible [7]. In fact, while all pollutant emissions increase with altitude, the NOx emission depends on the EGR ratio so that it is able to be kept at low levels while the boost system is below its mechanical limits [17]. Thus, the negative impact that altitude and common control strategies bring to emissions produces greater dependence on the correct selection and sizing of the aftertreatment system, as underlined by Haohao et al. [18] in the analysis of a light-duty Diesel engine emissions as a function of the altitude.

In view of the importance of the ambient conditions on the engine performance and emissions, the thermal management of the ATS has become fundamental, as addressed by Hamedi et al. [19], who discussed the importance of exhaust energy storage to improve the pollutants conversion efficiency, or Luján et al. [20], who explored the potential of exhaust thermal insulation. Thus, the calibration and design efforts for altitude and ambient temperature boundaries are gaining in importance. The traditional strategies to deal with these tasks have been related to costly, low repeatable real driving test campaigns or the use of altimetric chambers, which provided a good solution for steady altitude at the expense of low test cell availability and high cost due to building investment and energy consumption. Faced with the necessity of overcoming the drawback of these testing methods, different atmosphere simulator concepts have been proposed. Already back in 1990, a high altitude simulator was developed by Human et al. [21] to provide reduced atmospheric pressure to both the intake and the exhaust of a heavy-duty Diesel engine. This way, the analysis of the engine response can be performed when working at different altitudes overcoming the main disadvantages of traditional methodologies. In this sense, a more versatile concept was described by Testa [22], who proposed two root compressors connected to the intake and exhaust of the engine to set the working pressure to a higher or lower value that the ambient one in the test facility. Desantes et al. developed a Multi function Efficient Dynamic Altitude Simulator (MEDAS) [23,24] based on a mobile concept to reproduce the ambient pressure as a function of the altitude at the inlet and outlet of internal combustion engines [25]. In addition, MEDAS can be coupled to different modules for temperature and humidity control to provide an integral atmosphere simulation. The use of this altitude simulator has been validated against an altimetric test cell [26] comparing a complete engine mapping under steady-state conditions. Its ability to deal with transient operation has been also tested running driving cycles at constant altitude [14] and reproducing driving conditions with variable altitude [26].

Alternatively, the modelling softwares have become a key tool for powertrain design. They can provide a prediction against different boundary conditions and strategies and, at the same time, a comprehensive understanding on the processes governing the changes in performance. Numerous studies have been conducted exploring different modelling categories, as exposed by Sujesh et al. [27]. The benefits of modelling arise in noticeable savings in development time and costs while providing the possibility to try new calibrations and layouts without any risk for the engine [28]. In this perspective, modelling becomes a very valuable option for studies in variable altitude and ambient temperature. Taking as starting point the use of the altitude simulator as the main feature of the testing facility, the aim of this paper is to propose a 1D model able to simulate the performance of a Diesel engine and the aftertreatment system operating at different ambient temperature and pressure. The model is developed in GT-Power environment with externally user-defined turbocharger and aftertreatment sub-modules. This tool is to contribute to the need to have available a reliable performance evaluation and basic settings during the engine pre-design and calibration stages. Therefore, the predictive capability of the model is assessed by exploring different ambient conditions. Particular focus is put on the modelling of the combustion, the turbocharger and the exhaust aftertreatment system, which accounts for a DOC and a wall-flow particulate filter (DPF). From the model calibration at sea-level, new combustion and boost pressure settings are defined to maximise the engine torque while meeting mechanical limits. Next, the obtained flow boundaries are applied to the analysis of the DOC performance in terms of CO and HC emission as well as to the discussion on the DPF equilibrium point and filtration efficiency as a function of the particulate size distribution (PSD).

Experimental setup

In this work, an Euro6d-Temp serial production passenger car engine has been considered as a baseline for the validation of the proposed model in terms of performance and emissions. The more relevant characteristics of the engine are listed in Table 1.

The engine was coupled to an asynchronous dynamometer to control the engine speed and torque and to the altitude simulator, which was composed of MEDAS [25] and MEDAS Temperature Module (MTM). The test cell was equipped with a open engine control unit (ECU) to modify the engine calibration when required via ETAS INCA software. In this study the SOI, the injected fuel mass flow and the variable geometry turbine (VGT) position were modified looking for the maximum torque in full-load conditions as a function of altitude and ambient temperature, as forward discussed. As sketched in Fig. 1, the engine was instrumented with sensors to measure the main magnitudes defining the engine and aftertreatment performance: temperature and pressure along the air path,

Table 1
Main characteristics of the engine.

Engine type	HSDI Diesel
Emission standards	Euro6d-Temp
Number of cylinders	4 in line
Displaced volume [cm^3]	1461
Bore [mm]	76
Stroke [mm]	80.5
Number of valves	2 per cylinder
Compression ratio	15.16 : 1
Rated power @ speed	81 kW @ 4000 rpm
Rated torque @ speed	260 Nm @ 1750 rpm
Fuel injection	Common-rail direct injection
Turbocharger	VGT
EGR	HP-& cooled LP-EGR

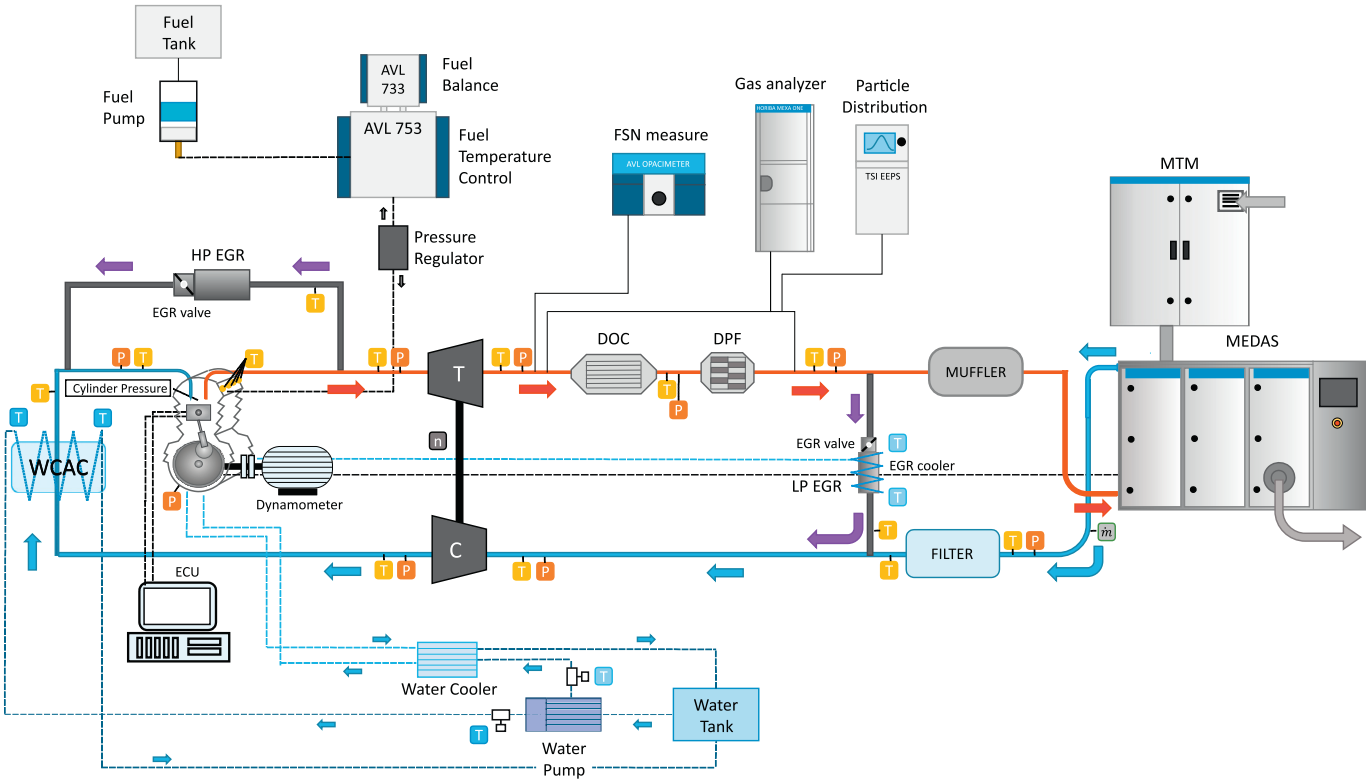

Fig. 1. Scheme of the engine test cell.

air and fuel mass flow, in-cylinder pressure, engine speed, engine torque, turbocharger speed and pollutant emissions. Additionally, an external circuit was employed to provide coolant flow to the engine, the low pressure EGR (LP-EGR) cooler and the water charge air cooler (WCAC).

The measurement of the pollutant emissions was performed with three different devices. The gaseous emissions were monitored with a Horiba Mexa-One gas analyser measuring upstream and downstream of the exhaust aftertreatment system alternatively in order to compute the CO and HC conversion efficiency. The particulate matter emission was measured with an AVL 439 opacimeter placed upstream of the ATS and with a TSI Engine Exhaust Particle Sizer (EEPS) employed to determine the total particle concentration and its size distribution. The TSI EEPS was coupled to a valve system allowing the alternative measurement upstream and downstream of the DPF in order to provide a figure of the DPF filtration efficiency as a function of the particle size. The main geometrical parameters of the DOC and DPF are defined in Table 2.

Modelling tools and calibration procedure

The core of the modelling approach is a 1D gas-dynamic model of the engine developed in GT-Power [29] environment. GT-Power is used to predict engine performance quantities such as power, torque, air mass flow, volumetric efficiency, fuel consumption, turbocharger performance and matching, and pumping losses, among others. The complete gas path from the engine inlet until the tailpipe exhaust conditions was completely modelled in GT-POWER.

Table 2
Main DOC and DPF geometric parameters.

	DOC	DPF
Diameter [mm]	120	170
Monolith length [mm]	140	80
Channel cross-section	Square	Square
Cell density [cpsi]	400	400
Cell size [mm]	1.04	0.95
Wall thickness [mm]	0.23	0.32
Catalytic area [m^2]	3.95	
Filtration area [m^2]		2.1
Porosity [−]		0.40
Mean pore diameter [μm]		20.4
Permeability [$\times 10^{13} m^2$]		7.59

The baseline model has been improved by substituting some default sub-models by user functions coming from OpenWAM™, which is an open-source gas dynamics software for internal combustion engines and components computation developed at CMT-Motores Térmicos [30,31]. In particular, the turbocharger and aftertreatment sub-models have been replaced as next described.

As a first stage of the modelling work, the engine model calibration was performed looking for a consistent balance between measured and modelled results. This way, Fig. 2 shows the good ability of the model to predict the engine performance in full-load conditions from low to high engine speed. Table 3 summarises the main boundaries and governing parameters of the calibration procedure leading to these results.

Firstly, the environmental conditions are defined. On this regard, it is important to note that MEDAS + MTM define the engine inlet temperature in the experimental setup, being it different to the room temperature. However, the model has not the possibility to distinguish between these temperatures, i.e. the room temperature is assumed as the inlet engine temperature and is used as boundary condition to compute the heat losses to the ambient. As a solution, the room temperature was imposed as inlet condition to define the heat transfer boundary for the model. In addition, a cooler was placed in the model next to the engine intake. This cooler did not involve any pressure drop but allowed to set the tested engine intake temperature, i.e. the one with which the air mass flow really enters the engine. Following the flow path, the boost pressure is regulated by means of a PID acting on the VGT position. The intake flow conditions are finally set imposing the flow temperature at the WCAC outlet. With respect to the combustion process, both the fuel mass flow and the SOI were imposed as boundary conditions. Also regarding the engine block, the air mass flow and the turbine inlet temperature are dependent on a fine tuning of the heat transfer coefficients of the intake

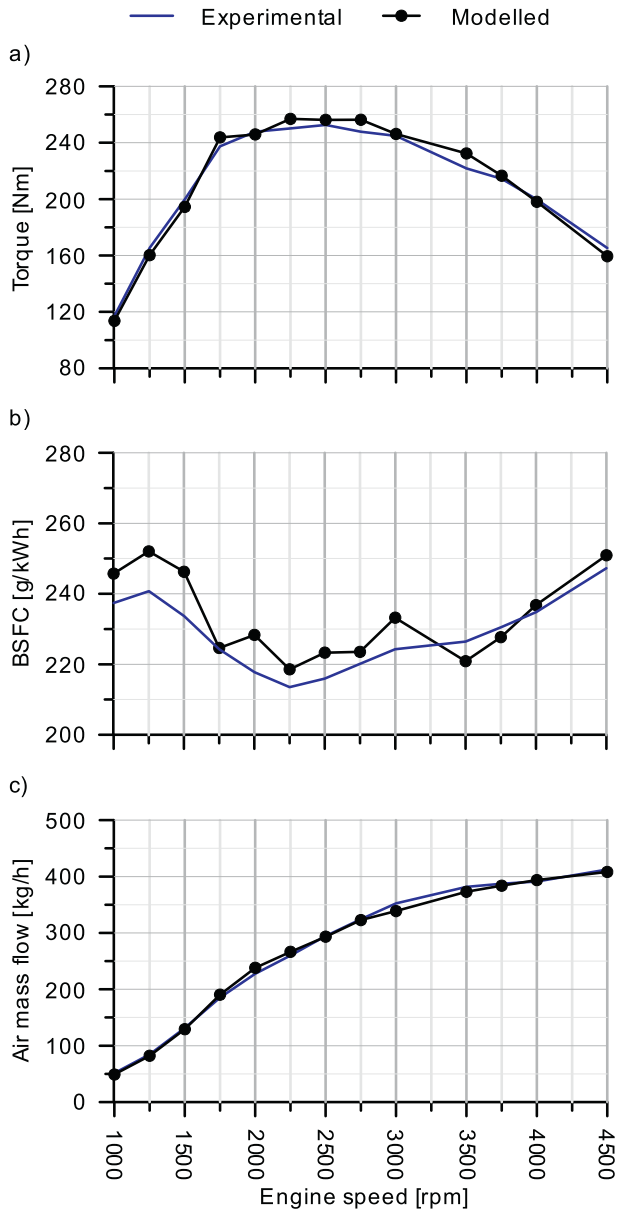

Fig. 2. Comparison between experimental and modelled torque, BSFC and air mass flow in full-load conditions.

Table 3
Main parameters for engine model calibration.

Room temperature	Imposed
Ambient temperature	Imposed
Ambient pressure	Imposed
Intake manifold temperature	Imposed
Engine speed	Imposed
Fuel mass flow	Imposed
SOI	Imposed
Exhaust gas composition	Imposed
Boost pressure	PID on VGT position
Air mass flow	Intake ports heat transfer coef.
Turbine inlet temperature	Exhaust ports heat transfer coef.

and exhaust ports. Since this work has been focused on full-load operating conditions being the EGR paths closed. Concerning the modelling of the ATS, the gas composition has been imposed from experimental data at the DOC inlet for the modelling of CO, HC and soot abatement from the thermo-and fluid-dynamic properties predicted by the engine model.

Combustion sub-model

The modelling of the instantaneous in-cylinder pressure was performed applying the DIPulse [32] predictive combustion model from GT-Power, which predicts the combustion rate for direct-injection Diesel engines with single and multi-pulse injection profiles. The basic approach of this model is to track the fuel as it is injected, evaporates, mixes with surrounding gas, and burns. This model discretises three thermodynamic zones, each with their own temperature and composition within the cylinder: the unburned zone, which contains the in-cylinder mass at intake valve closing; the spray unburned zone, which comprises the injected fuel and the entrained gas; and the spray burned zone, which is composed of the combustion products. The model covers the computation of the gas entrainment rate, the ignition delay, the premixed combustion rate and the diffusion combustion rate to predict the in-cylinder pressure trace. Fig. 3 shows very good agreement between the experimental and modelled in-cylinder pressure and rate of heat release (RoHR) obtained at 1500 rpm and 4000 rpm.

The same degree of accuracy is obtained in the remaining engine speeds, whose results are summarised in Fig. 4 as a function of the combustion completeness and the maximum in-cylinder pressure. As observed, Fig. 4 (a) confirms that the combustion rate is accurate from the start of combustion to the late combustion phase providing a good prediction of the maximum in-cylinder pressure, as represented in Fig. 4(b). This is especially relevant for maximum torque calibration at different ambient conditions since it is closely related to maximum in-cylinder pressure.

Turbocharger sub-model

The engine model in GT-Power has been coupled to an advanced turbocharger model in order to properly consider the influence of the heat transfer [33] and mechanical losses [34] in the turbocharger on the

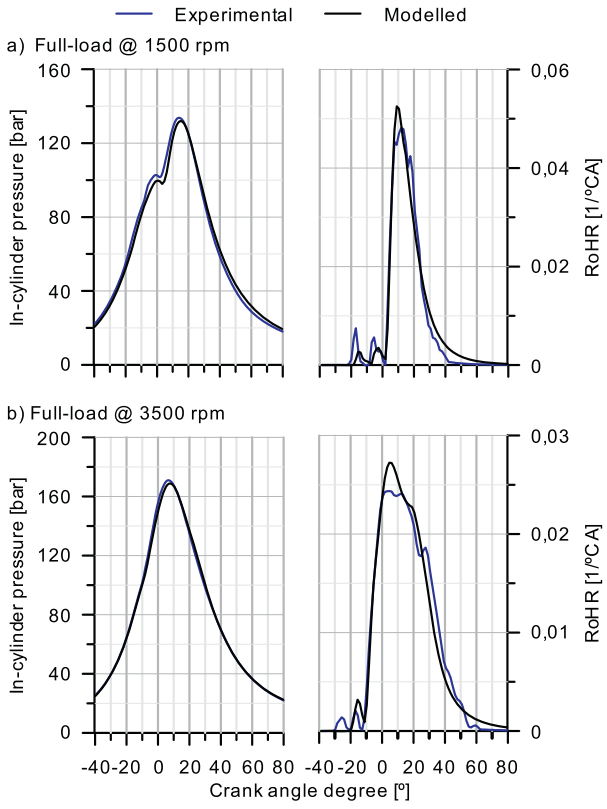

Fig. 3. Comparison between experimental and modelled in-cylinder pressure and rate of heat release at full-load at 1500 rpm and 4000 rpm.

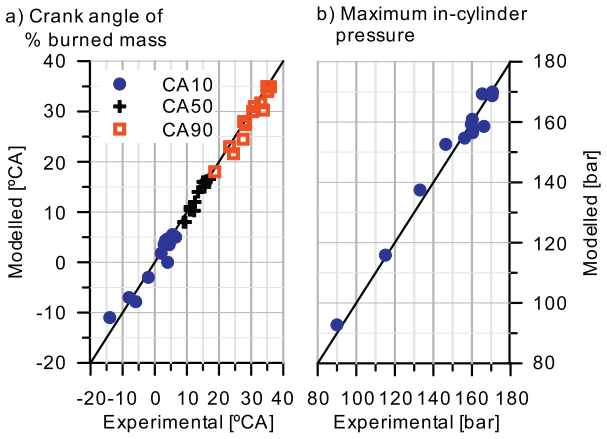

Fig. 4. Prediction of combustion completeness and maximum in-cylinder pressure at full-load conditions from 1000 rpm to 4500 rpm.

prediction of the engine performance and of exhaust gas properties [20]. The turbine extracts energy from the exhaust gas flow, which is used to drive the compressor accounting for the mechanical losses. The heat balance is closed with the heat losses from the turbine and its transmission from the turbine case across the turbocharger until it reaches the compressor. This heat flux is partly rejected to the lubricating and cooling systems. In the compressor side, the air exchanges heat with the compressor casing [35].

Fig. 5 represents the comparison between experimental and modelled turbocharger characteristic variables. Plot (a) shows the prediction of the turbocharger speed and its evolution towards values close to its upper limit as the engine speed increases, being the gap accurately predicted by the model. Similarly, plot (b) focuses on working pressures. The prediction of the compressor outlet pressure validates the pressure drop in the intake line because of the intake manifold pressure control with the VGT position, as commented in Section 3. The good prediction of the combustion process and the computation of the heat fluxes across the turbocharger also leads to a good agreement in gas temperature both in the compressor and turbine stations.

Aftertreatment sub-model

A lumped approach is used in this work to model the response of the aftertreatment system, which consists of a close-coupled brick composed of a DOC and a DPF. The DOC model [36] solves the pressure drop, heat transfer and chemical mechanism processes based on a modular approach as sketched in Fig. 6.

The pressure drop is computed assuming incompressible flow across the catalyst, so that it is a function of the inlet gas density and velocity as well as a pressure drop coefficient dependent on the catalyst geometry and the Reynolds number [37]. Therefore, the gas dynamic model sets the mass flow across the monolith, which conditions the heat transfer and the reactions rate. The heat transfer from the gas to the substrate and the environment is solved applying an adaptation of a bi-dimensional lumped nodal approach for monolithic reactors [38]. The nodal network is simplified to neglect the axial heat transfer so that provides the outlet gas temperature and a mean value of the substrate temperature in the whole monolith taking into account convection from gas to substrate, radial heat conduction towards the metal canning and final radiation and convection to the environment as well as the thermal capacity of every material and the heat released by the chemical reactions. Governed by the substrate temperature, the DOC model accounts for CO and HC abatement. Their rate of oxidation and adsorption are computed by solving the one-dimensional chemical species transport equations under the assumption of quasi-steady flow [9],

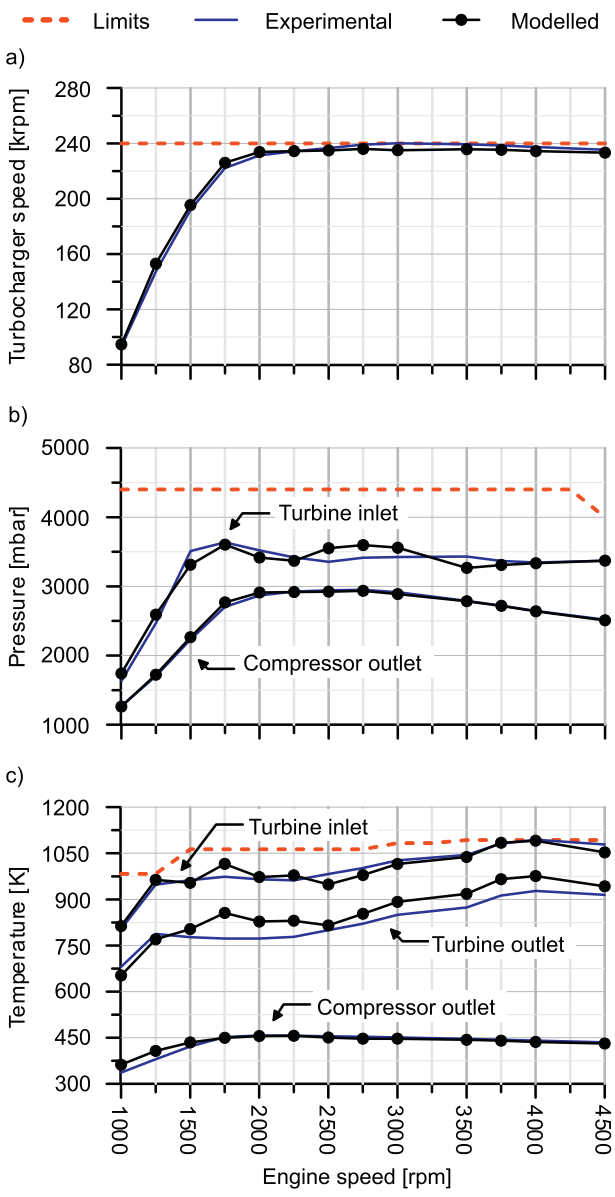

Fig. 5. Comparison between experimental and modelled speed, pressures and temperatures in the turbocharger at full-load conditions from 1000 rpm and 4500 rpm.

$$u_{in}\frac{dX_n}{dx} = -S_{p,cat}k_{m,n}(X_n - X_{n,wc}) \quad (1)$$

$$\sum_j \nu_n R_{j,n} + S_{p,wc}k_{m,n}(X_n - X_{n,wc}) = 0, \quad (2)$$

where Eq. (1) represents the bulk gas equation and Eq. (2) accounts for the chemical species transport in the washcoat of the pollutant species *n*. This system of equations for every chemical species is integrated within a control volume where the pollutants are assumed to be the limiting species, i.e. other reactants are assumed to be constant within the control volume during the resolved time-step. In a chemical mechanism focused on CO and HC oxidation, this hypothesis applies to O_2, whose concentration in the exhaust mass flow is high in comparison to CO and HC under lean combustion conditions [36]. Therefore, the outlet concentration of species *n* can be finally determined by directly integrating along the monolith length [9].

The DOC outlet gas properties determine the boundaries for the DPF modelling. As in the case of the DOC, a mean value DPF model is

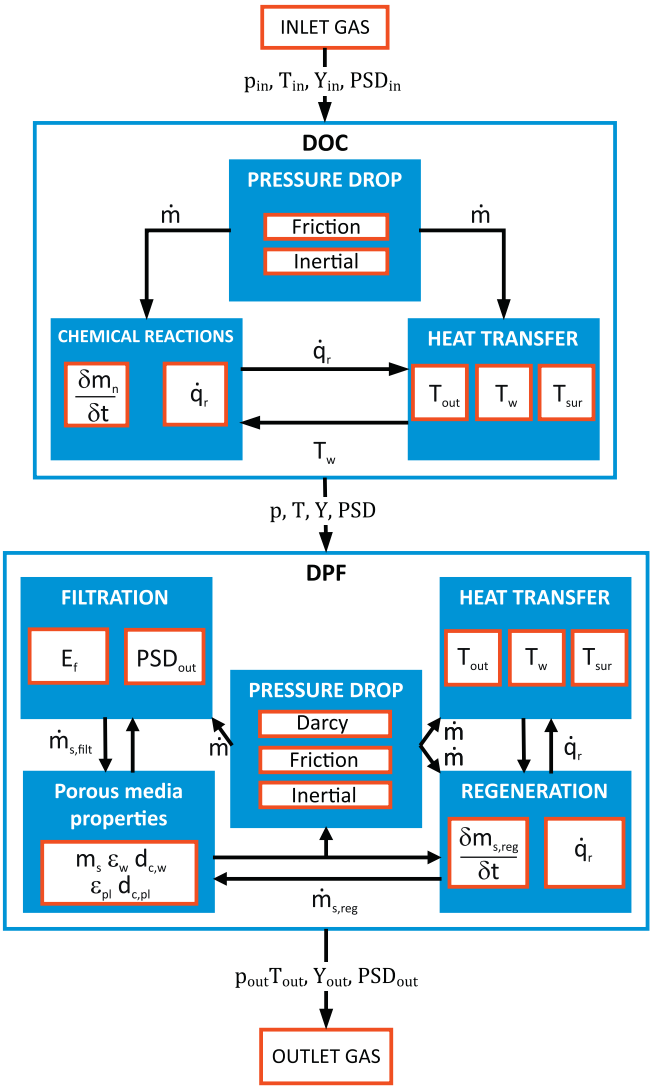

Fig. 6. Flow-chart of DOC and DPF sub-models.

considered in this work. It computes the main physical and chemical processes governing the DPF response, i.e. pressure drop, heat transfer, soot filtration, regeneration and the change in meso-and micro-geometry of the inlet channels and the porous medium due to particulate matter accumulation.

According to Fig. 6, the DPF model calculates the soot mass accumulated into the DPF from the filtration to soot oxidation balance. In turn, the amount of soot into the DPF conditions the dynamics of the filtration efficiency and the regeneration as well as the pressure drop response. Eq. (3) represents the soot mass variation rate within the monolith:

$$\frac{\delta m_s}{\delta t} = \frac{\delta m_{s,filt}}{\delta t} - \frac{\delta m_{s,reg}}{\delta t} \tag{3}$$

On the one hand, the amount of oxidised soot mass is computed by means of a regeneration sub-model that accounts for the soot reactivity with O_2 and NO_2 as

$$\frac{\partial m_{s,reg}}{\partial t} = M_C \left(-\frac{1}{\alpha_{NO_2}} \frac{\partial n_{NO_2}}{\partial t} - \frac{1}{\alpha_{O_2}} \frac{\partial n_{O_2}}{\partial t} \right), \tag{4}$$

where the depletion rate of every gaseous reactant is obtained from the solution of the 1D transport equation of chemical species across every porous medium layer [39],

$$u_w \frac{\partial X_n}{\partial z} = -\left(S_{p,ext} + \eta_{int_n} S_{p,int}\right) \alpha_n k_n \frac{K_{S_n} p_n}{1 + K_{S_n} p_n} \tag{5}$$

where the subscript n identifies the reactant species.

On the other hand, the amount of filtrated soot mass is computed from the prediction of the overall filtration efficiency. Besides, the filtration sub-model calculates the filtration efficiency as a function of the particle size. In particular, the Brownian diffusion and interception mechanisms are considered in this work to determine the filtration efficiency around an isolated single collector being the inertial contribution neglected [40].

The Brownian diffusion mechanism is the governing mechanism for small size particles increasing its contribution as the filtration velocity decreases. The filtration efficiency for a single unit collector due to Brownian diffusion is obtained according to Eq. (6):

$$\eta_D = 3.5 \left(\frac{\varepsilon_w}{K}\right)^{\frac{1}{3}} Pe_w^{-\frac{2}{3}} \tag{6}$$

The Peclet number is a function of the filtration velocity, the micro-geometry of the loaded porous medium and the particle diffusivity. The soot load is the main governing parameter of the collection process leading to high filtration efficiency. Nevertheless, the flow properties have important effects when the soot loading is low. Its influence is mainly related to the mass flow and the gas temperature. The gas temperature directly affects the particle diffusion coefficient according to Eq. (8) [41]. In addition, the gas density is also affected leading to a relevant influence on the filtration velocity at constant mass flow.

$$Pe_w = \frac{u_w d_{c,w}}{\varepsilon_w D_s} \tag{7}$$

$$D_s = \frac{T K_B S C F_w}{3\pi\mu d_s}, \tag{8}$$

Complementary to Brownian diffusion, the interception mechanism takes importance as the particle size increases. This mechanism is related to the ability of the particles to follow the streamline until they are adhered on the external surface of a unit collector. The interception efficiency of a single sphere is quantified according to Lee and Gieseke [41] as

$$\eta_R = 1.5 \frac{N_R^2}{1 + N_R^{\frac{3-2\varepsilon_w}{3\varepsilon_w}}} \frac{\varepsilon_w}{K}, \tag{9}$$

where N_R is the interception parameter defined as the particle size to unit collector diameter ratio.

Finally, the filtration efficiency of an isolated single collector is obtained applying the independence rule to consider the mutual effect of both mechanisms:

$$\eta_{DR} = \eta_D + \eta_R - \eta_D \eta_R \tag{10}$$

The filtration efficiency of an isolated single collector is considered to determine the overall efficiency of the packed bed of spherical particles composing the porous wall by integrating within the control volume [42]:

$$E_{f,w} = 1 - e^{-\frac{3\eta_{DR}(1-\varepsilon_w) w_w f_w S_c}{2\varepsilon_w d_{c,w}}}, \tag{11}$$

Fig. 7 represents the main results summarising the DOC response in these tests. In particular, Fig. 7(a) compares the experimental and modelled DOC pressure drop and outlet temperature, which show a very good agreement in the whole tested range.

The CO and HC conversion efficiencies are shown in Fig. 7(b). Table 4 shows the chemical kinetics calibration of the tested DOC and DPF devices obtained from the full-load tests. The model is able to reproduce both the orders of magnitude of the conversion efficiency for both

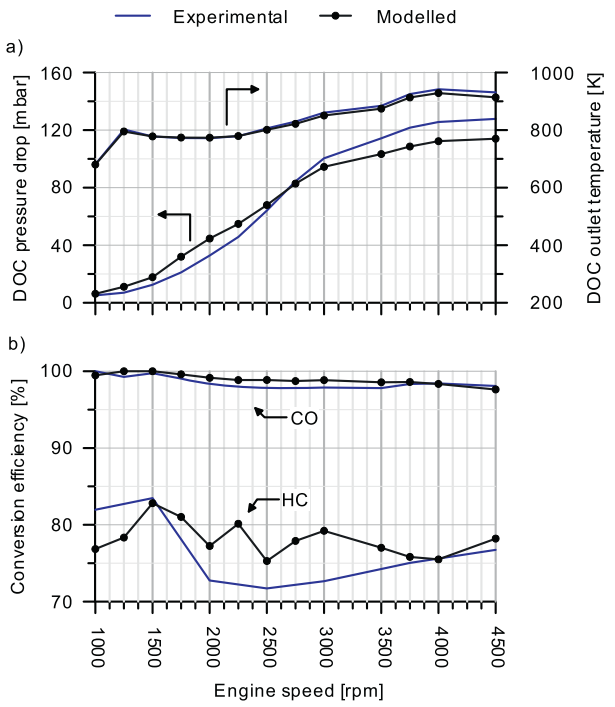

Fig. 7. Comparison between experimental and modelled DOC pressure drop, outlet gas temperature and conversion efficiency.

pollutants, close to 100% in the case of CO and within the range 70–80% for unburned HC. On this regard, the model shows high sensitivity to predict the mass transfer limitations in the case of CO, which are evidenced in the reduction of the conversion efficiency as the dwell time gets reduced due to the mass flow (Fig. 2(c)) and exhaust gas temperature (Fig. 5(c)) increase.

The performance of the DPF model is represented in Fig. 8. Plot (a) in Fig. 8 confirms the good ability of the ATS models to capture the thermo- and fluid-dynamic response in honeycomb monoliths. In the particular case of a wall-flow monolith, the pressure drop is directly dependent on the determination of the balance point between soot filtration and oxidation. Since all points were measured after 30 min of thermal stabilisation, the loading and passive regeneration processes were simulated as a way to properly predict the experimental DPF pressure drop and outlet gas temperature. Fig. 9(a) represents the full-load at 1500 rpm, which is almost to reach the balance point with constant pressure drop as the profile of filtrated and regenerated soot mass equal their slopes. This operating point is taken next as baseline for the analysis at different altitudes and ambient temperatures in Section 4. As a complementary result of the filtration process, Fig. 9(b) shows the filtration efficiency as a function of the PSD corresponding to this operating points. Despite the fact that the model slightly underestimates the PSD filtration efficiency from 40 nm to 400 nm, the model captures with high accuracy the most penetrating particle size, which is close to 160 nm as result of the Brownian diffusion to inertial contribution trade-off.

Altitude and ambient temperature variation

Four different altitude and ambient temperature combinations were tested at 1500 rpm maximising the torque as a validation of the model in variable ambient conditions. The boundaries for every tested point are detailed in Table 5, which also includes the baseline full load at 1500 rpm named as #A. The torque was maximised for every altitude and ambient temperature by re-calibrating the injected fuel mass, SOI and boost pressure at the same time as the engine was kept below the opacity (12.5%) and mechanical limits. In particular, the maximum in-

Table 4
DOC and DPF kinetic parameters.

DOC	CO oxidation	A_n $[s^{-1}]$	2.0×10^{17}
		E_{a_n} [J/mol]	1.05×10^{5}
	HC oxidation	A_n $[s^{-1}]$	1.1×10^{18}
		E_{a_n} [J/mol]	1.25×10^{5}
	HC adsorption	A_n $[s^{-1}]$	2.2
		E_{a_n} [J/mol]	0
	HC desorption	A_n $[s^{-1}]$	1.0×10^{4}
		E_{a_n} [J/mol]	1.05×10^{5}
DPF	O_2	A_n $[m/s]$	6×10^{-3}
		E_{a_n} [J/mol]	9×10^{4}
	NO_2	A_n $[m/s]$	8×10^{-3}
		E_{a_n} [J/mol]	8.5×10^{4}

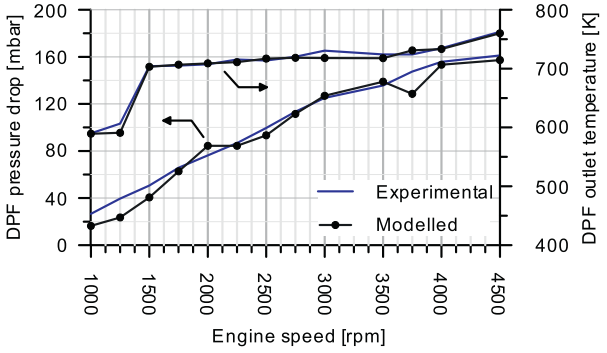

Fig. 8. Comparison between experimental and modelled DPF pressure drop and outlet gas temperature.

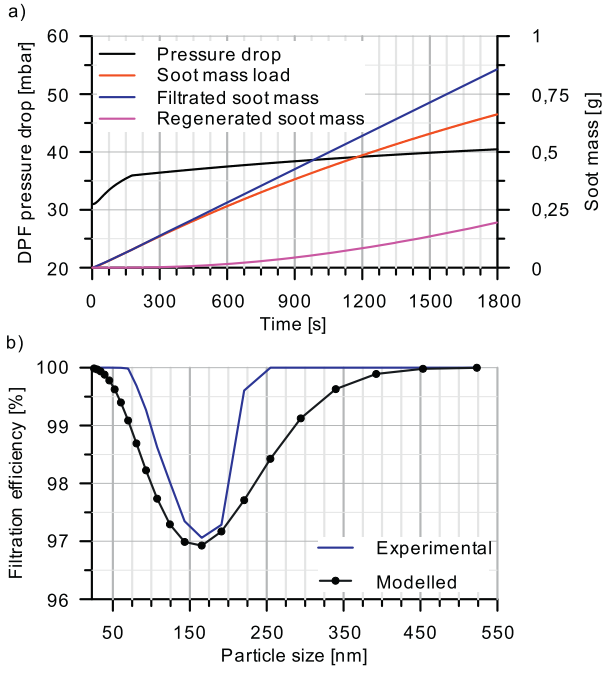

Fig. 9. Filtration and passive regeneration equilibrium and filtration efficiency as a function of the PSD in full-load at 1500 rpm.

cylinder pressure and pressure gradient were reached being the VGT almost fully closed.

As shown in Fig. 10, the model is able to provide high accuracy in the prediction of the engine performance and air mass flow. With respect to the baseline sea level calibration at 20°C, the heat transfer coefficients in

Table 5
Altitude and ambient temperature cases tested at full-load at 1500 rpm.

Point ID	Altitude [m]	T_{amb} [°C]	p_{amb} [bar]	Torque
#A	0	20	1.013	Baseline
#B	0	20	1.013	Maximum
#C	0	8	1.013	Maximum
#D	2500	20	0.75	Maximum
#E	2500	8	0.75	Maximum

the intake and exhaust ports were needed to be modified according to fitted correlations dependent on the intake and exhaust manifold conditions, respectively.

Besides the equivalence ratio increase observed in all optimised cycles (Fig. 10(c)), the improvement to torque brought to sea level cases is in part due to a slight opening of the VGT, as shown in Fig. 11(a). By acting this way, the boost pressure barely changes for 20°C due to the increase in turbine efficiency and even increases at 8°C while the air mass flow also does increases, as represented in Figs 10(c) and 11(b) respectively. At the same time, it contributes to reduce the pumping losses as well as to be kept below the limit in turbine inlet temperature (Fig. 11(c)).

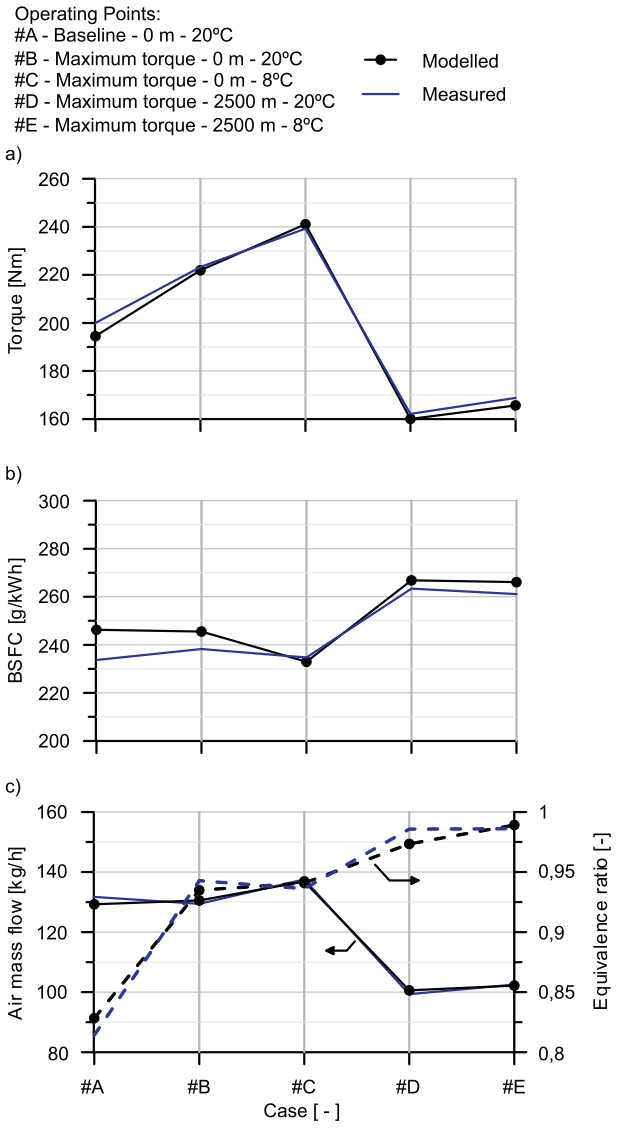

Fig. 10. Comparison between experimental and modelled results at full-load at 1500 rpm for different ambient conditions.

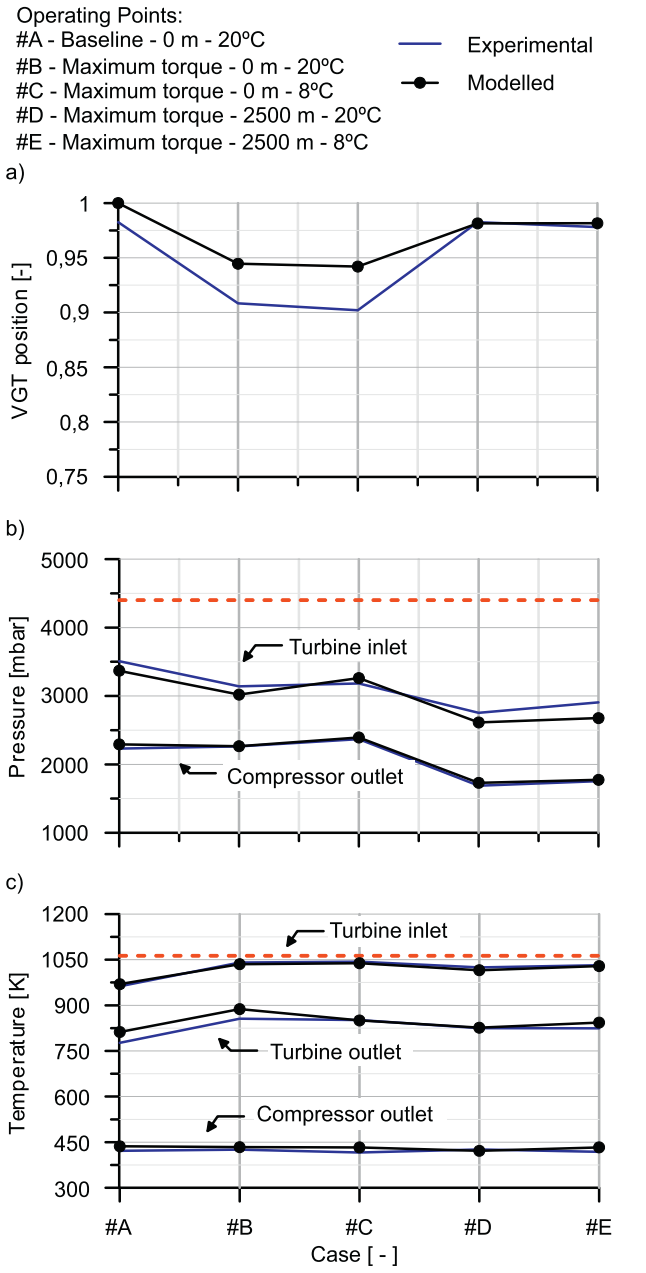

Fig. 11. Comparison between experimental and modelled VGT position, pressures and temperatures in the turbocharger at full-load at 1500 rpm for different ambient conditions.

However, the VGT has to be closer at 2500 m looking for the maximum boost pressure and air mass flow as a way to reach the maximum torque at these extreme driving conditions. The less amount of air damages the torque. Nevertheless, the trade-off is slightly balanced since it is possible to move the equivalence ratio almost to stoichiometric conditions and advance the combustion till meeting the limit in maximum in-cylinder pressure.

The maximisation of the full load torque has an impact on the engine raw emissions but also on the tailpipe ones because of the change in the ATS performance. In particular, Fig. 12(a) shows the CO and HC conversion efficiency for every tested altitude and ambient temperature case. In cases #B and #C at sea level a reduction in CO and HC conversion efficiency from 100% to 80% in baseline conditions to 70% and 40% in maximised torque cases. Since mass flow and gas temperature are almost invariant, as previously shown in Figs. 10 and 11, the reason for this response is to be found in the change in gas composition. The increase of

the equivalence ratio reduces the amount of available O_2 to very low levels and hence the CO and HC oxidation rate. Nonetheless, this is not the governing phenomenon. The new combustion setup leads the CO concentration to increase in a relevant manner. Therefore, both CO and HC oxidation become inhibited [43]. This phenomenon leads to almost null CO and HC conversion efficiency at 2500 m. At this altitude, the combination of further increase of equivalence ratio and lower boost pressure results in the reduction of O_2 concentration to 0.5% and the CO concentration over 10000 ppm. Consequently, the oxidation rate diminishes because of the reduction in the kinetic term and the increase of the inhibition one.

The response of the DPF becomes also affected by the change in altitude and ambient temperature at maximum torque. In comparison to the baseline case #A, whose DPF pressure drop along the stabilisation is shown in Figs. 9 and 13 evidences that the DPF pressure drop increases in cases #B to #D. Only case #B seems to reach an steady value after 30 min but 10 mbar greater than case #A. The reason is the increase in soot emission, which delays the filtration to passive regeneration equilibrium. Despite the fact that case #C has similar fluid-dynamic conditions, the higher mass flow and soot emission avoids to reach the balance point between filtration and soot oxidation. This is even clearer at 2500 m cases, whose pressure drop slope is almost constant due to the very low soot oxidation rate governed by the low O_2 concentration. In these conditions, it is also relevant to note that the pressure drop is increased by the lower exhaust gas density caused by the higher altitude. This is evident in case #D, which provides a similar pressure drop than sea level cases despite the low exhaust mass flow and the lowest filtrated soot mass due to the lowest emission. In the same way, case #E, which is characterised by similar soot emission than cases #B and #C, causes the highest DPF pressure drop.

Summary and conclusions

In this work a 1D gas dynamic model has been described and validated for different intake temperature and pressure conditions. The performance of the proposed model relies on a precise calibration of the combustion process as well as on the turbocharger and aftertreatment sub-models, which were included as a user-defined functions into GT-Power. This way, the model was firstly calibrated for full load conditions at sea level and 20°C with good and balanced accuracy concerning magnitudes related to combustion, air management and emissions abatement. On this last concern, both gas and particulate matter abatement were covered modelling a DOC and DPF brick. The model is focused on pressure drop, heat transfer and gas phase reactions in the catalyst as well as soot filtration as a function of the particle size distribution and passive regeneration in the wall-flow monolith.

Departing from a baseline calibration, the model was excited with four air intake conditions including pressure and temperature variation. It was tested coupling the engine to the altitude simulator MEDAS. Precise results have been obtained by the model for the re-calibration of the injected fuel mass, SOI and boost pressure to maximise the engine torque at the different ambient conditions taking care of mechanical operational limits. The model is able to predict the change in torque and BSFC besides air flow properties both in the intake and the exhaust line, even at very high altitude with ambient temperature sensitivity.

The strategy to keep maximum torque for full-load conditions has evidenced a relevant damage to the ATS performance at sea level and, especially, as the altitude increases. It is mainly due to the increase of the equivalence ratio towards stoichiometric conditions. Despite the presence of O_2 in the exhaust gas in a concentration ranging from 0.5% to 1.5%, its low value decreases the kinetic term for CO and HC oxidation. Nevertheless, the governing factor for the loss of conversion efficiency is the huge increase in CO concentration, which is over 10000 ppm at 2500 m. Such a concentration inhibits the oxidation reactions leading

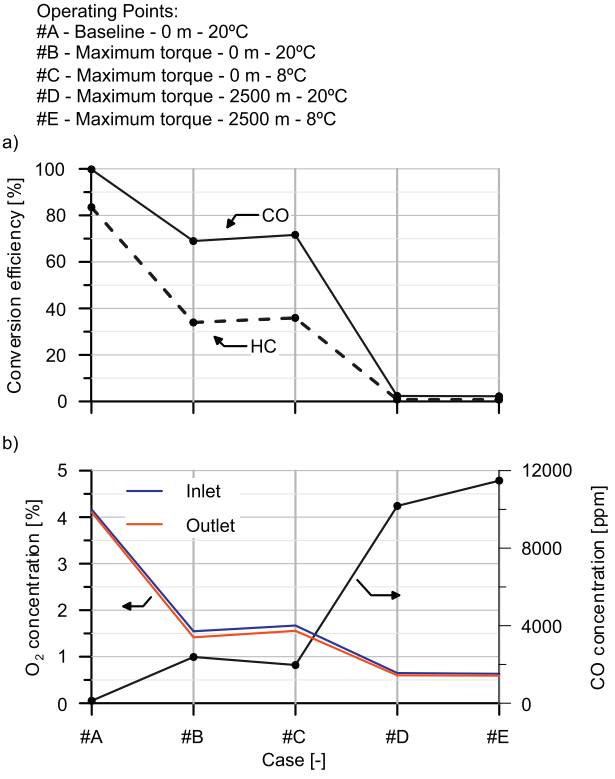

Fig. 12. DOC response at full-load at 1500 rpm for different ambient conditions.

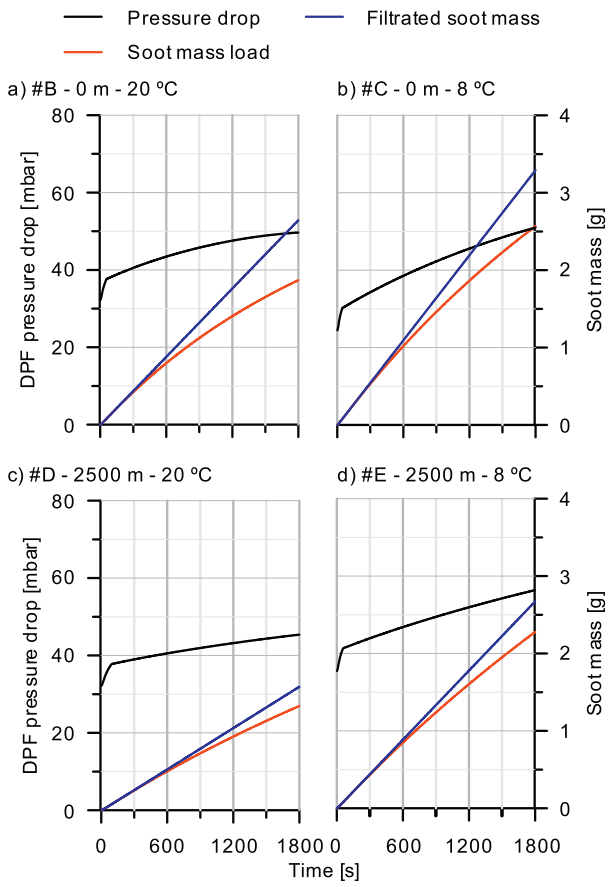

Fig. 13. DPF response during stabilisation at full-load at 1500 rpm for different ambient conditions.

even to cancel the DOC function. It evidences the need to consider new design guidelines for the ATS because of cold high altitude constraints or to add further limits to torque maximisation based on equivalence ratio limits. Similarly, the DPF is also highly affected by operating at low O_2 concentration. On the one hand, the torque maximisation increases the soot emission with respect to the baseline case. Nevertheless, all ambient boundaries were showing a similar emission. The low O_2 availability and the high soot emission resulted in a delay in the balance point between filtration and passive regeneration despite the high exhaust gas temperature at full load. As a consequence, the DPF pressure drop increases continuously at constant slope. In addition, the lower exhaust gas density as the driving altitude increases damages the pressure drop and penalises further the engine performance.

Conflict of interest

The authors declare that they have no known competing financial interests or personal relationships that could have appeared to influence the work reported in this paper.

Acknowledgements

This research has been partially supported by FEDER and the Government of Spain through project TRA2016-79185-R. Additionally, the Ph.D. student Bárbara Diesel has been funded by a grant from the Government of Generalitat Valenciana with reference ACIF/2018/109.

References

[1] Commission Implementing regulation (EU) ../.. of 2.6.2017 Setting Out a Methodology for Determining the Correlation Parameters Necessary for Reflecting the Change in the Regulatory Test Procedure with Regard to Light Commercial Vehicles and Amending Implementing Regulation (EU) No 293/2012, June 2017.
[2] C. Dardiotis, G. Martini, A. Marotta, U. Manfredi, Low-temperature cold-start gaseous emissions of late technology passenger cars, Appl. Energy 111 (2013) 468–478.
[3] J. Ko, D. Jin, W. Jang, C.L. Myung, S. Kwon, S. Park, Comparative investigation of NOx emission characteristics from a Euro 6-compliant Diesel passenger car over the NEDC and WLTC at various ambient temperatures, Appl. Energy 187 (2018) 652–662.
[4] L. Cédric, M. Goriaux, P. Tassel, P. Perret, M. André, Y. Liu, Impact of aftertreatment device and driving conditions on black carbon, ultrafine particle and nox emissions for Euro 5 Diesel and gasoline vehicles, Transp. Res. Proc. 14 (2016) 3079–3088.
[5] Delphi Technologies, Worldwide Emissions Standards: Passenger Cars and Light Duty Vehicles 2018-2019, 2018.
[6] N. Hooftman, M. Messagie, J. Van Mierlo, T. Coosemans, A review of the European passenger car regulations. Real driving emissions vs local air quality, Renew. Sustain. Energy Rev. 86 (2018) 1–21.
[7] J.R. Serrano, P. Piqueras, A. Abbad, R. Tabet, S. Bender, J. Gómez, Impact on reduction of pollutant emissions from passenger cars when replacing Euro 4 with Euro 6d Diesel engines considering the altitude influence, Energies 12 (2019) 1278–1301.
[8] J.M. Luján, H. Climent, L.M. García-Cuevas, A. Moratal, Pollutant emissions and diesel oxidation catalyst performance at low ambient temperatures in transient load conditions, Appl. Therm. Eng. 129 (2018) 1527–1537.
[9] P. Piqueras, A. García, J. Monsalve-Serrano, M.J. Ruiz, Performance of a diesel oxidation catalyst under diesel-gasoline reactivity controlled compression ignition combustion conditions, Energy Convers. Manag. 196 (2019) 18–31.
[10] M.V. Faria, R.A. Varella, G.O. Duarte, T.L. Farias, P.C. Baptista, Engine cold start analysis using naturalistic driving data: city level impacts on local pollutants emissions and energy consumption, Sci. Total Environ. 630 (2018) 544–559.
[11] C. Weber, I. Sundvor, E. Figenbaum, Comparison of regulated emission factors of Euro 6 LDV in Nordic temperatures and cold start conditions: diesel- and gasoline direct-injection, Atmos. Environ. 206 (2019) 208–217.
[12] J. Ko, J. Son, C. Myung, S. Park, Comparative study on low ambient temperature regulated/unregulated emissions characteristics of idling light-duty Diesel vehicles at cold start and hot restart, Fuel 233 (2018) 620–631.
[13] J. Ko, C. Myung, S. Park, Impacts of ambient temperature, DPF regeneration and traffic congestion on NOx emissions from a Euro 6-compliant diesel vehicle equipped with an LNT under real-world driving conditions, Atmos. Environ. 200 (2019) 1–14.
[14] V. Bermúdez, J.R. Serrano, P. Piqueras, J. Gómez, S. Bender, Analysis of the role of altitude on Diesel engine performance and emissions using an atmosphere simulator, Int. J. Engine Res. 18 (2017) 105–117.
[15] A. Ramos, R. García-Contreras, O. Armas, Performance, combustion timing and emissions from a light duty vehicle at different altitudes fueled with animal fat biodiesel, GTL and diesel fuels, Appl. Energy 182 (2016) 507–517.
[16] L. Shen, Y. Shen, Combustion process of diesel engines at regions with different altitude, SAE Technical Paper 950857 (1995), https://doi.org/10.4271/950857. Paper 950857.
[17] Y. Linxiao, G. Yunshan, T. Jianwei, H. Chao, W. Xuezhi, L. Hao, Z. Wei, G. Jiadong, F. Geng, F. Xiangyu, W. Xin, Experimental investigation of the impact of biodiesel on the combustion and emission characteristics of a heavy duty Diesel engine at various altitudes, Fuel 115 (2014) 220–226.
[18] W. Haohao, G. Yunshan, H. Lijun, X. Xiaoliu, T. Jianwei, L. Jiachen, W. Legang, Y. Jia, Y. Dongxia, P. Jian, Y. Jin, Y. Rong, The real driving emission characteristics of light-duty Diesel vehicle at various altitudes, Atmos. Environ. 191 (2018) 126–131.
[19] M.R. Hamedi, O. Doustdar, A. Tsolakis, J. Hartland, Thermal energy storage system for efficient diesel exhaust aftertreatment at low temperatures, Appl. Energy 235 (2019) 874–887.
[20] J.M. Luján, J.R. Serrano, P. Piqueras, B. Diesel, Turbine and exhaust ports thermal insulation impact on the engine efficiency and aftertreatment inlet temperature, Appl. Energy 240 (2019) 409–423.
[21] D.M. Human, T.L. Ullman, T.M. Baines, Simulation of high altitude effects on heavy-duty diesel emissions, SAE Tech (1990), https://doi.org/10.4271/900883. Paper Series.
[22] D. Testa, Apparatus and Method for Altimetric Conditioning of Internal Combustion Engines, Patent EP2295950B1, May 2013.
[23] J.M. Desantes, J. Galindo, F. Payri, P. Piqueras, J.R. Serrano, Device for Atmosphere Conditioning for Testing Combustion Engines, and Associated Method and Use, Patent WO 2015/110683 A1, July 2015.
[24] J.M. Desantes, J. Galindo, F. Payri, P. Piqueras, J.R. Serrano, Device for Conditioning the Atmosphere in Test of Alternative Internal Combustion Engines, Method and Use of Said Device, July 2016. Patent WO 2016/116642 A1.
[25] J. Galindo, J.R. Serrano, P. Piqueras, J. Gómez, Description and performance analysis of a flow test rig to simulate altitude pressure variation for internal combustion engines testing, SAE Int. J. Engines 7 (4) (2014) 1686–1696.
[26] A. Broatch, V. Bermúdez, J.R. Serrano, R. Tabet, J. Gómez, S. Bender, Analysis of passenger car turbocharged Diesel engines performance when tested at altitude and of the altitude simulator device used, in: Proceedings of the ASME 2018 Internal Combustion Engine Division Fall Technical Conference, 2018, https://doi.org/10.1115/1.4043395. San Diego, CA, USA.
[27] G. Sujesh, S. Ramesh, Modeling and control of Diesel engines: a systematic review, Alexandria Eng. J. 57 (2018) 4033–4048.
[28] H. Koegeler, G. Regner, T. Sams, K. Gschweitl, Using simulation and optimization tools to decide engine design concepts, in: SAE Tech. Paper, 2000, https://doi.org/10.4271/2000-01-1267, 2000-01-1267.
[29] GAMMA technologies. www.gtisoft.com, June 2019.
[30] OpenWAM Webpage, CMT-Motores Térmicos, Universitat Politècnica de València, June 2019. www.openwam.org.
[31] J. Galindo, J.R. Serrano, F.J. Arnau, P. Piqueras, Description of a semi-independent time discretization methodology for a one-dimensional gas dynamics model, J. Eng. Gas Turbines Power 131 (3) (2009) 034504–034508.
[32] Gtisoft.com, Applications. [Online] Available at: http://www.gtisoft.com/applications/a_Engine_Performance.php, 2015.
[33] J.R. Serrano, P. Olmeda, F.J. Arnau, A. Dombrovsky, et al., Analysis and methodology to characterize heat transfer phenomena in automotive turbochargers, J. Eng. Gas Turbines Power 137 (2) (2015) 021901–021911.
[34] J.R. Serrano, P. Olmeda, F.J. Arnau, A. Dombrovsky, Turbocharger heat transfer and mechanical losses influence in predicting engines performance by using one-dimensional simulation codes, Energy 86 (2015) 204–218.
[35] J.R. Serrano, P. Olmeda, A. Páez, F. Vidal, An experimental procedure to determine heat transfer properties of turbochargers, Meas. Sci. Technol. 21 (3) (2010) 035109–035122.
[36] F. Payri, F.J. Arnau, P. Piqueras, M.J. Ruiz, Lumped approach for flow-through and wall-flow monolithic reactors modelling for real-time automotive applications, SAE Tech (2018), https://doi.org/10.4271/2018-01-0954. Paper 2018-01-0954.
[37] A.J. Torregrosa, J.R. Serrano, F.J. Arnau, P. Piqueras, A fluid dynamic model for unsteady compressible flow in wall-flow diesel particulate filters, Energy 36 (2011) 671–684.
[38] J. Galindo, J.R. Serrano, P. Piqueras, O. García-Afonso, Heat transfer modelling in honeycomb wall-flow diesel particulate filters, Energy 43 (2012) 201–213.
[39] V. Macián, J.R. Serrano, P. Piqueras, E.J. Sanchis, Internal pore diffusion and adsorption impact on the soot oxidation in wall-flow particulate filters, Energy 179 (2019) 407–421.
[40] J.R. Serrano, H. Climent, P. Piqueras, E. Angiolini, Filtration modelling in wall-flow particulate filters of low soot penetration thickness, Energy 112 (2016) 883–898.
[41] K.W. Lee, J.A. Gieseke, Collection of aerosol particles by packed beds, Environ. Sci. Technol. 13 (4) (1979) 466–470.
[42] B. Logan, D.G. Jewett, R.G. Arnold, E.J. Bouwer, C. O'Melia, Clarification of clean-bed filtration models, J. Environ. Eng. 121 (1995) 869–873.
[43] S.H. Oh, J.C. Cavendish, Transients of monolithic catalytic converters. Response to step changes in feedstream temperature as related to controlling automobile emissions, Ind. Eng. Chem. Prod. Res. Dev. 21 (1982) 29–37.

Nomenclature

A_n: pre-exponential factor of the oxidation reaction with reactant n
c_{gas}: gas flow molar concentration
d_c: unit collector diameter
d_s: soot particle diameter

D_s: Soot diffusion coefficient
E_{a_n}: activation energy of oxidation reaction with reactant n
E_f: filtration efficiency
f_w: penetrated fraction of porous wall thickness
k: permeability
k_n: kinetic constant of the oxidation reaction with species n
K: Kuwabara's hydrodynamic factor
K_B: Boltzmann constant
K_{S_n}: equilibrium constant of adsorption process of species n
$\dot{m}_n$: mass flow of species n
m_s: soot mass
$m_{s,reg}$: regenerated soot mass
M: molar mass of chemical species
n_n: molar rate of species n
N_R: interception parameter
^{p}: gas pressure
p_{amb}: ambient pressure
p_n: partial pressure of species n
Pe: Peclet number
$\dot{q}_r$: power released by soot oxidation
$r_{p,s}$: pore radius of soot primary particle
$\Re$: universal gas constant
S_p: soot specific surface
S_c: sticking coefficient
SCF: Stokes-Cunningham factor
t: time
T_{amb}: ambient temperature
T_w: substrate temperature
u: gas velocity
u_w: filtration velocity
w_w: porous wall thickness
X: molar fraction
Y: mass fraction
Greek letters
α_n: completeness index of reactant n
ε: porosity
η_D: Brownian efficiency
η_{DR}: single unit collector efficiency
η_{int}: diffusion efficiency
η_R: interception efficiency
κ: thermal conductivity
μ: dynamic viscosity
ν: stoichiometric coefficient
θ_n: Langmuir isotherm of reactant n
ρ: density
τ_s: normalised soot depletion rate
$\dot{\omega}_n$: reaction rate of reactant n
Acronyms
1D: one-dimensional
ATS: exhaust aftertreatment system
BSFC: brake specific fuel consumption
CA10: crank angle at 10% of burned mass
CA50: crank angle at 50% of burned mass
CA90: crank angle at 90% of burned mass
DOC: diesel oxidation catalyst
DPF: diesel particulate filter
EGR: exhaust gas recirculation
EEPS: engine exhaust particle sizer
HP-EGR: high pressure exhaust gas recirculation
LNT: lean NOx trap
LP-EGR: low pressure exhaust gas recirculation
MEDAS: multi function efficient dynamic altitude simulator
MTM: MEDAS temperature module
PID: proportional-integral-derivative controller
PSD: particle size distribution
RDE: real driving emissions
RoHR: rate of heat release
SOI: start of the injection
VGT: variable geometry turbine
WCAC: water charger air cooler
WLTC: worldwide harmonized light vehicles test cycle
WLTP: worldwide harmonized light-duty vehicles test procedure
Subscripts
c: referred to collector unit
ext: referred to soot particle external properties
filt: referred to filtration
in: referred to ATS inlet
int: referred to soot particle internal properties
n: referred to gaseous reactant
out: referred to ATS outlet
reg: referred to regeneration
s: referred to soot
w: referred to porous wall